

Alma Mater Studiorum Università di Bologna  
Archivio istituzionale della ricerca

Parametric Detection and Classification of Compact Conductivity Contrasts With Electrical Impedance Tomography

This is the final peer-reviewed author's accepted manuscript (postprint) of the following publication:

*Published Version:*

Parametric Detection and Classification of Compact Conductivity Contrasts With Electrical Impedance Tomography / Samorè, Andrea; Guermandi, Marco; Placati, Silvio; Roberto Guerrieri. - In: IEEE TRANSACTIONS ON INSTRUMENTATION AND MEASUREMENT. - ISSN 0018-9456. - STAMPA. - 66:10(2017), pp. 7954985.2666-7954985.2679. [10.1109/TIM.2017.2711818]

*Availability:*

This version is available at: <https://hdl.handle.net/11585/627027> since: 2018-02-27

*Published:*

DOI: <http://doi.org/10.1109/TIM.2017.2711818>

*Terms of use:*

Some rights reserved. The terms and conditions for the reuse of this version of the manuscript are specified in the publishing policy. For all terms of use and more information see the publisher's website.

This item was downloaded from IRIS Università di Bologna (<https://cris.unibo.it/>).  
When citing, please refer to the published version.

(Article begins on next page)

This is the final peer-reviewed accepted manuscript of:

A. Samorè, M. Guermandi, S. Placati and R. Guerrieri, "**Parametric Detection and Classification of Compact Conductivity Contrasts With Electrical Impedance Tomography**" in *IEEE Transactions on Instrumentation and Measurement*, vol. 66, no. 10, pp. 2666-2679, Oct. 2017

The final published version is available online at:

<https://doi.org/10.1109/TIM.2017.2711818>

Rights / License:

The terms and conditions for the reuse of this version of the manuscript are specified in the publishing policy. For all terms of use and more information see the publisher's website.

This item was downloaded from IRIS Università di Bologna (<https://cris.unibo.it/>)

**When citing, please refer to the published version.**

# Parametric detection and classification of compact conductivity contrasts with Electrical Impedance Tomography

Andrea Samorè, Marco Guermandi, Silvio Placati, Roberto Guerrieri

**Abstract**—Electrical Impedance Tomography (EIT) is a non-invasive and cost effective imaging method which is increasingly attractive in the field of medical diagnostics. Several health conditions, such as stroke and solid tumors are characterized by compact conductivity anomalies surrounded by a fairly regular background. Commonly employed voxel by voxel reconstruction methods for impedance imaging share the disadvantages of high computational cost and substantial sensitivity to measurement noise and imperfections in the electrical model describing the domain of interest. We present a special purpose algorithm for automatic detection and identification of compact conductivity variations. The technique exploits a-priori structural information and, by reconstructing only the limited number of parameters required to describe a compact conductivity contrast, does not depend on a critical regularization parameter. The most demanding kernels are implemented to run on Graphics Processing Units (GPUs) to accelerate computation. The parametric reconstruction is quicker and more robust than widely employed approaches with respect to measurement noise and imperfections in the electrical model, as shown by computational analysis performed on a segmented head domain and experimental measurements acquired on a cylindrical phantom. When the goal is quick detection of compact conductivity contrasts in complex 3D domains, the inclusion of specific constraints relating to the problem considered leads to enhanced quality of reconstruction, making the presented technique a promising alternative to common voxel by voxel reconstruction methods.

**Index Terms**—Impedance imaging, Impedance tomography, Biomedical imaging, Detection algorithms, Inverse problems.

## I. INTRODUCTION

**E**LECTRICAL Impedance Tomography is a non-invasive and cost effective imaging method in which an impedance map of the region of interest is reconstructed from measured electric potentials generated by current injections. The technique has been applied in a wide variety of fields, spanning from geoelectrical imaging [1] to industrial process monitoring [2], robotics [3] and biomedical imaging [4].

Focusing on the biomedical setting, a number of EIT acquisition systems have been developed in the past by various research groups, with several intended applications that span from the monitoring of ventilation [5] and gastric emptying [6] to the detection of solid tumors [7],[8] and localization of cerebral activity [9]. Recent developments include the realization

of active electrodes which can be used to alternatively measure potentials or inject current at the same spot [10], increasing the portability of the system and its flexibility in terms of current-injection patterns available, which increases the accuracy of reconstruction.

Very often, as in the case of solid tumors, diagnosis of localized variation in blood perfusion or identification of intracerebral strokes, the goal consists in the detection and approximate localization of a compact conductivity variation that is surrounded by an electrically fairly uniform background tissue. Due to the nature of the diagnosis process, baseline measurements (healthy state) are generally not available. For this reason, time difference (TD) imaging is not an option and absolute or frequency difference (FD) algorithms, which are more sensitive to modeling and measurement errors when compared to TD [11], must be employed.

In what follows, stroke will be considered as a case study to illustrate the performance of the proposed solution on complex domains since it is known to alter the conductivity of brain tissues in a predictable way: during ischemia the decreased extracellular volume due to cellular swelling (cytotoxic edema) reduces the average conductivity of the region affected [12]; on the other hand, when intracranial bleeding occurs, the average conductivity of the flooded region increases significantly due to blood being more conductive than cerebral tissue [13]. Early recognition is crucial for therapy since, if an ischemic condition is detected within 4.5 hours of onset, it is possible to initiate treatment with Tissue Plasminogen Activator (tPA), a clot-busting therapeutic agent [14]. At the same time, discrimination is fundamental since treatment of a hemorrhagic condition by tPA may well result in additional damage to the patient [15].

Impedance imaging of stroke is a challenging task which requires great precision in the description of the electrical model of the head and very accurate acquisition systems. Previous endeavours, many of which took advantage of multifrequency measurements in an attempt to reduce the impact of various systematic sources of noise, failed to yield reproducible results due to limitations in the accuracy of instrumentation, and significant and not easily avoided uncertainties in the electrical model of the head [16]. Another factor that hampers the application of FD techniques to the detection of hemorrhagic conditions is the very weak dependency of blood impedance with respect to frequency [17]. Bayesian approximation error approaches have been applied in the past to reduce the effect of uncertainty in the external boundary of the volume of interest

The authors are with the Advanced Research Center on Electronic Systems (ARCES), University of Bologna, Bologna 40123, Italy (e-mail: andrea.samore@unibo.it).

This work was partially funded by the CREAM project. The CREAM project received funding from the European Union under the Seventh Framework Programme, grant agreement no. 612022.

in absolute reconstructions [18][19] and to increase contrast in simple 2D models of the head [20], but their extension to a complex 3D domain describing accurately the main layered tissues of the human head is not straightforward and the computational cost of the inversion step remains significant. Although EIT systems specifically designed to image stroke have been developed [21], the image reconstruction problem continues to be strongly underdetermined and remarkably sensitive to measurement and discretization noise.

The aim of this work is to propose an algorithm for automatic detection and classification of compact conductivity variations based on an approach specifically tailored to the application. This approach reduces the ill-posedness of EIT inversion by avoiding the need to reconstruct a complete absolute conductivity map of the domain of interest on a voxel by voxel basis. Instead, reconstruction of regions of uniform conductivity, representing the various underlying tissues, is separated from the detection of a compact conductivity variation, so that only a small number of parameters are estimated at each iteration of the nonlinear algorithm. While the proposed approach shares some similarities with previously described methods [22], [23], to the best of the authors' knowledge a parametric reconstruction algorithm able to quickly detect and classify an unspecified number of compact conductivity inclusions in realistic 3D complex domains, when significant uncertainty in the electrical model and measurement noise are present, is not reported in the literature.

The proposed parametric technique proves to be quicker, devoid of a critical regularization parameter and resilient to errors in the electrical model of the domain of interest.

EIT requires intense processing of the measured data, so the critical kernels of the algorithm presented are tailored to heterogeneous parallel systems based on multiple CPUs and GPUs. A workstation equipped with Graphics Processing Units (GPUs) allows for small-scale supercomputer performances with off the shelf components [24], bringing the advantages of limited cost, size and energy consumption [25].

This work is structured as follows. Section II introduces the novel approach to EIT reconstruction and compares it to a more standard automatic method based on Tikhonov regularized inversion; Section III details the implementation of both algorithms; Section IV deals with characterization of their performance in the presence of various noise sources and conclusions are drawn in Section V.

## II. ALGORITHMS

In order to reconstruct an impedance map of the region of interest, two different computational modules must be in place: a forward and an inverse problem solver [26]. The forward problem solver is used to compute the voltage distribution in the volume of interest, given the applied current and the physical properties of the domain. The forward problem formulation stems from the Poisson problem in the quasi-static case with Neumann boundary conditions [27] (system of equations 1).

$$\begin{cases} -\nabla \cdot \sigma \nabla \phi = 0 & \text{on } \Omega \\ \iint_{S_i} \sigma \nabla \phi \cdot \hat{n} dS = \iint_{S_i} g \cdot \hat{n} dS = I_i & \text{with } i = 1 \cdots N_e \\ \sigma \nabla \phi \cdot \hat{n} dS = 0 & \text{on } \Omega / \cup_{i=1}^{N_e} S_i \end{cases} \quad (1)$$

where  $\sigma$  is the local conductivity of the medium and  $\phi$  is the local electric potential. One convenient approach is to assume  $\sigma$  to be piecewise constant in each voxel of the discretized volume  $\Omega$ . In the second and third equation,  $g$  is the local current density,  $\hat{n}$  is the versor normal to the surface of the electrode, and  $I_i$  is the current injected in the  $i$ -th electrode of area  $S_i$ . The second equation defines the current that flows through each of the  $N_e$  electrodes placed on the scalp. The third one specifies that there is no current flow across the boundary where injecting electrodes are not present.

The inversion method makes use of the forward problem solver to provide an estimate of the physical properties of the volume given the stimulation pattern and the set of measurements. For our purposes, the domain under analysis can be considered to be composed of five different tissues: scalp, skull, connective tissue, cerebrospinal fluid (CSF) and brain.

Early attempts to reconstruct images from impedance measurements include the backprojection algorithm [28], which is derived from the Radon transform used in computed tomography, and the Landweber method, which can be considered a modification of the generalized inverse matrix method [29]. Commonly used inversion methods typically reconstruct a conductivity map of the region of interest by estimating the conductivity of each voxel of the discretized domain and, due to the ill-posedness of the inverse problem, nowadays generally aim to minimize a least square functional which is regularized by adding a penalty term. Different regularization methods have been developed in the past by several research groups. The L2-norm is arguably the most widely used method in practice, it enhances the stability of reconstruction by penalizing steep impedance variations. Several options for the regularization matrix are available, from the identity matrix [30], approximations of differential operators [31] and matrices based on structural priors [32]. Tikhonov regularization (TR) is a prime example of a L2-norm method. Other regularization methods, such as Total Variation [33] and sparsity regularization [34],[35] employ a L1-norm in an attempt to enhance the reconstruction of piecewise constant conductivity distributions. Subdomain methods have been used to enhance reconstruction accuracy by either including prior structural information or by limiting the image reconstruction process to a specific subregion of interest inside the domain [36],[37],[38]. A different class of reconstruction methods based on a statistical approach that takes into account modeling errors has been the focus of recent research [18],[19]. In the following, the proposed approach will be compared to an implementation of TR, the most commonly employed method which is also generally used as a benchmark to test the performance of new EIT reconstruction algorithms [34],[39].

The idea behind the algorithm which we propose is that, given the prior information provided by the specific problem,



it is not necessary to reconstruct a conductivity map of the volume of interest on a voxel by voxel basis, because the main goal is to detect a compact conductivity anomaly, classify it as an increase or decrease in conductivity with respect to the background and be able to approximately identify its volume without focusing on the exact shape of the variation. For this reason we adopt a Parametric Approach to Reconstruction (PAR), in which a conductivity distribution containing an anomaly characterized by a first-guess position, size and conductivity variation associated with a stroke condition is iteratively modified in its properties up to two possible results. If the algorithm converges to a feasible location and size for the anomaly, a target is identified. Otherwise, no irregularity is detected.

#### A. Parametric Algorithm

In order to grasp the basic concept underpinning the proposed algorithm, we describe it first in a simplified 2D domain where we consider a uniform disc of conductivity  $\sigma_0$  containing a punctiform target anomaly having a small variation in conductivity with respect to the background (see Fig.1). Sixteen equally spaced electrodes are placed on the boundary of the domain. Each electrode can be used to inject current or to measure potential and the injection pattern consists of 8 different opposite injections. Previous research demonstrated that an opposite injection pattern allows for better reconstruction quality in presence of measurement noise and when the anomalies that need to be detected are far from the electrodes i.e. in the central region of the phantom [40]. For this reason, in the following only the opposite injection pattern will be considered. In this simple setup with 16 electrodes the number of independent opposite current injections is 8 and, since for each current injection 2 of the electrodes are used to inject current and one is used as a reference, the number of measurements is 104 [41]. Considering the first injection, the current enters the domain from electrode 1 and exits from electrode 9. In the second injection the input and output electrodes are numbers 2 and 10, and so on. For each injection, all the non-injecting electrodes are measuring surface potentials.

In this domain, for each injection, the forward problem takes the form  $-\sigma \nabla^2 \phi = 0$ , with Neumann boundary conditions. The solution can be computed analytically to be:

$$\begin{cases} \phi(r, \theta) = \sum_{n=0}^{\infty} r^n \cdot [A_n \cdot \cos(n\theta) + B_n \cdot \sin(n\theta)] \\ A_0 = \text{free} \quad , \quad A_n = \frac{1}{\pi n R_0^{n-1}} \cdot \int_0^{2\pi} k(\theta) \cos(n\theta) d\theta \\ B_n = \frac{1}{\pi n R_0^{n-1}} \cdot \int_0^{2\pi} k(\theta) \sin(n\theta) d\theta \end{cases} \quad (2)$$

Where  $R_0$  is the radius of the disk and  $k(\theta)$  are the boundary conditions:

$$\begin{cases} k(\nu) = -1 \quad , \quad \nu = \frac{\pi}{8}, \frac{3\pi}{8}, \dots, (1 - \frac{1}{8})\pi \\ k(\nu + \pi) = 1 \end{cases} \quad (3)$$

To reconstruct the position of the target anomaly, we consider a punctiform guess conductivity variation, placed at an arbitrary point of the domain; the objective of the solver is to update the position of the guess till it converges on that of the

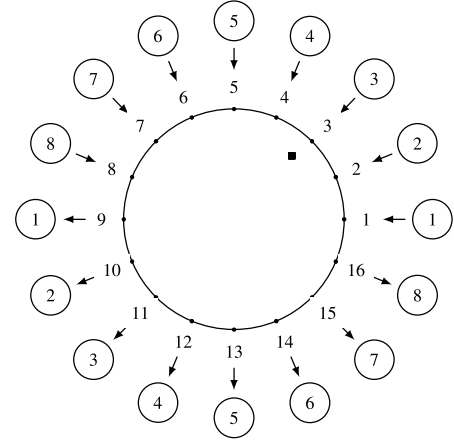


Fig. 1. 2D domain of uniform conductivity containing a single-voxel target anomaly depicted as a black square. Electrode positions are marked by dots and each injection pattern is denoted by a circled number and a couple of arrows that indicate the direction of the current.

target. The most straightforward way to act is to minimize the error defined as the 2-norm of the difference between potentials at the electrodes when only the target anomaly is present,  $V_t$ , and the potentials computable when only the moving anomaly is placed in the first guess position,  $V_g$ :

$$E = \|V_t - V_g\|^2 \quad (4)$$

As the minimization problem is non-linear, one common practical approach is to formulate a linear approximation of the surface potentials,  $V_t = V_g + J_p \cdot \Delta p$ , where  $\Delta p = [\Delta x \ \Delta y]$  defines the variation of spatial coordinates and  $J_p = [J_{px} \ J_{py}]$  is the Jacobian that relates a variation of sampled surface potentials to a variation of spatial coordinates for the guess. Using an iterative solver based on such a linearized approach, the update at each step will be:

$$\Delta p = (J_p^T \cdot J_p)^{-1} \cdot J_p^T \cdot (V_t - V_g) \quad (5)$$

Since we assume that the conductivity variation  $d\sigma$  is small compared to the background value, we can write:

$$\begin{cases} V_t = V_0 + J \cdot \Delta\sigma(x - x_t, y - y_t) \\ V_g = V_0 + J \cdot \Delta\sigma(x - x_g, y - y_g) \\ J_{px}(x, y) = J(x + \Delta x, y) - J(x, y) \\ J_{py}(x, y) = J(x, y + \Delta y) - J(x, y) \end{cases} \quad (6)$$

where  $(x_t, y_t)$  is the position of the target,  $(x_g, y_g)$  is the position of the guess,  $\Delta\sigma(u, v) = d\sigma$  for  $u = v = 0$  and  $\Delta\sigma(u, v) = 0$  otherwise.  $V_0$  are the potentials sampled at electrode positions when both target and guess anomalies are absent ( $\sigma(x, y) = \sigma_0$ ). The Jacobian  $J_i(x, y) = \frac{dV_i}{d\sigma(x, y)}$ , that relates the potential variation at the  $i$ -th measuring electrode to the conductivity variation in  $(x, y)$ , can be efficiently computed by exploiting the reciprocity principle [42].

Computing  $\Delta p$  for each voxel, we generate bi-dimensional maps which indicate the direction in which the guess anomaly will be moved in the following iteration of the non-linear solver, for every position inside the domain. The presence of

a basin of attraction (Fig.2, left-hand column) is clear when the sign of the guessed conductivity variation matches that of the target, while a repulsor appears if the guess conductivity variation and the target are opposite in sign (Fig.2, right-hand column). The first and second row illustrate maps relating to two different locations of the target anomaly. One may obtain similar results with different target anomaly positions.

The complete algorithm follows the same principle but includes the 3D cartesian coordinates  $(x, y, z)$  and radius  $r$  of the guess anomaly and also the conductivity of the background tissues (scalp, skull, connective tissue, CSF and brain) as variables to be reconstructed. The evolving conductivity map initially contains a spherical anomaly (probe) placed at an initial guess position with a first-guess radius and conductivity variation. The spherical shape of the wandering probe approximates the generic structure of a compact conductivity contrast. It is important to note that the actual anomaly to be detected doesn't have to be spherical. Approximate prior information about the electrical properties of background tissues and targets to be detected is readily available in the literature [43],[44],[45], or in online databases such as [46], and the initial guess conductivities are based on the available data. Moreover, the initial guess dimension of the wandering probe is selected to be in a realistic range for the considered application of stroke detection and discrimination according to previous studies [47].

At each iteration, the update is computed from (5). In this case,  $\Delta p$  is a vector that contains the conductivity variation of each kind of tissue considered as a whole unit, the variation of the spatial coordinates of the center of the anomaly and the variation of its radius. The algorithm stops in the case of a convergent reconstruction, a divergent reconstruction or when the maximum number of iterations set by the user is reached. In a convergent reconstruction  $\Delta p$  drops below a threshold and, in particular, the reconstruction is stopped when the reconstructed variation of size and position of the probe at the  $n$ -th inversion step is smaller than the spatial discretization step of the domain. Whereas a reconstruction is considered divergent if during the iterative process the volume of the probe is reduced below a certain limit. As in rare cases the wandering probe might enter a closed cycle of spatial movement around the target contrast, an additional stopping criterion based on a user-specified maximum number of iterations is present to guarantee the termination of the search process in a finite amount of time. The main steps of the reconstruction algorithm are outlined in Fig. 3.

Focusing now on the case study considered, stroke detection and discrimination, as the head domain is complex and the error function may present several local minima, the space is sampled by placing the probe in four different initial guess positions inside the cerebral tissue.

For each location, to discriminate between an ischemic and a hemorrhagic stroke, two different reconstructions are run in parallel: in the first one, the conductivity of the probe is set so as to be equal to that expected for an ischemic stroke; while in the second one it matches that of a hemorrhagic stroke.

Once the 8 reconstructions have been obtained, they are ranked according to their residual error  $E$  and the reconstruction

with the lowest  $E$  (deepest minimum) is then chosen.

### B. Tikhonov Based Algorithm

The regularized reconstruction algorithm considered in this work is based on a standard approach in EIT imaging [31]. Since the problem in question is ill-posed, additional information must be employed to get a single solution in reconstructing of the conductivity of each voxel relating to the brain region. One practical way to regularize the problem consists in including an additional term in the error function:

$$E(\sigma) = \|V_m - V_g(\sigma)\|^2 + \|\Gamma \cdot \sigma\|^2 \quad (7)$$

where  $V_m$  are the measured surface potentials,  $V_g$  are the computed surface potentials with an initial guess conductivity distribution  $\sigma_0$  while the regularization matrix  $\Gamma = \lambda \cdot M$  is composed of a regularization parameter,  $\lambda$ , and a matrix  $M$  that is constructed as a discrete Laplacian filter to enhance the smoothness of the reconstruction [32]. This is done to penalize gradient variation and thus favor the reconstruction of compact contrasts. In the application considered, anatomical information is taken into account by restricting  $M$  and the reconstruction process to the tissues which may be affected by strokes, namely the brain and CSF.

Under the linear approximation [48],  $E$  is minimized by:

$$\Delta\sigma = (J^T \cdot J + \Gamma^T \cdot \Gamma)^{-1} \cdot (J^T \cdot (V_m - V_g)) + \Gamma^T \cdot \Gamma \cdot (\sigma_r - \sigma_n) \quad (8)$$

Where  $\Delta\sigma = \sigma_{n+1} - \sigma_n$  is the conductivity update,  $\sigma_r$  is a reference conductivity distribution and  $\sigma_n$  is the reconstructed conductivity distribution at step  $n$ . The Jacobian matrix  $J$  can be computed by exploiting the reciprocity principle as before.

Since the conductivity of a region affected by a stroke differs significantly from healthy tissue, an iterative reconstruction is employed. At each step, the Jacobian is calculated, the linearized problem is solved and the guess conductivity distribution  $\sigma_0$  is updated adding the calculated contribution  $\Delta\sigma$ . The algorithm stops when the relative variation of the residual between consecutive iterations drops below a threshold or a user-defined maximum number of iterations is reached.

To extract meaningful information out of the reconstructed conductivity map, it is necessary to ascertain the presence of a conductivity anomaly and, if found, to classify it as an increase or decrease of conductivity with respect to the background. For this reason, the output image is segmented by thresholding it, the result is then labeled and the volume of each recognized region is computed.

## III. IMPLEMENTATION

The reconstruction algorithms are developed in Matlab and are based on the optimized parallel forward problem solver for EIT developed by our research group in C and CUDA [49]. The solver is based on the finite volume method (FVM) for evaluating the PDE and uses a cubic mesh.

The inversion algorithms considered in this paper share one common part, the electrical model, consisting in volume definition, and differ in the Jacobian calculation and inversion loop. The flowchart is summarized in Fig. 4.

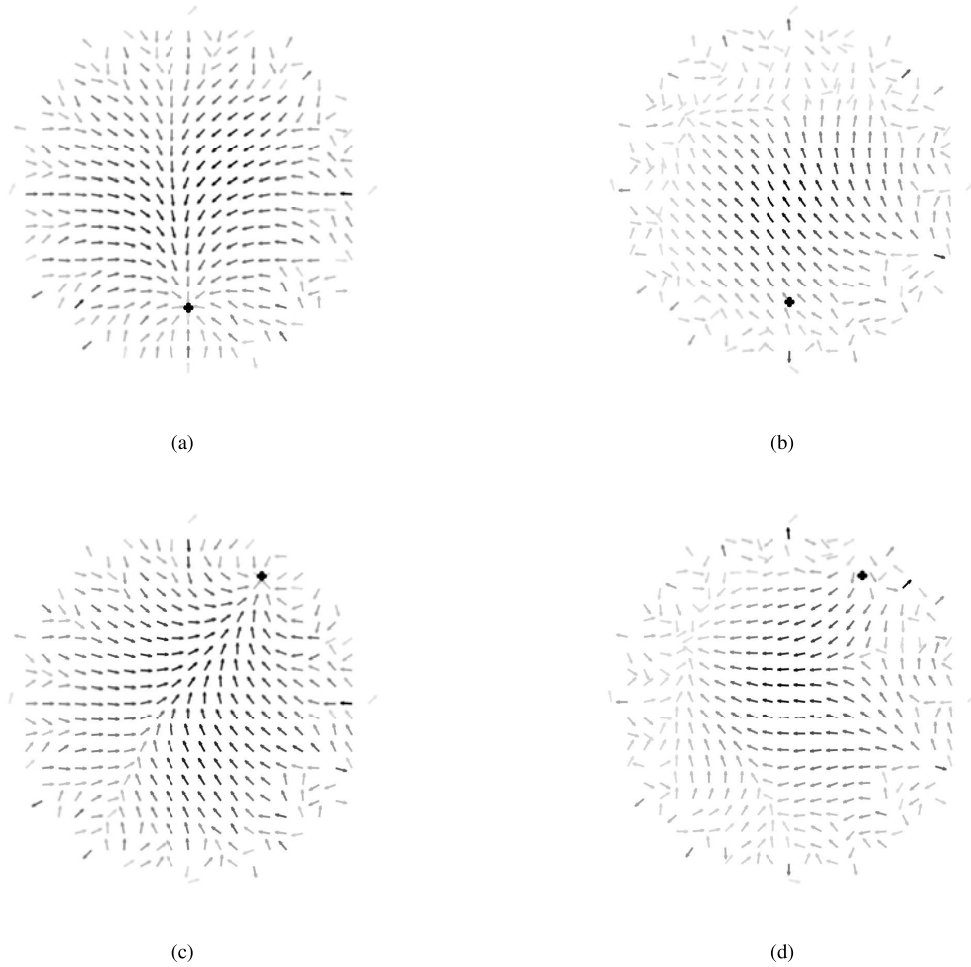


Fig. 2. Considering a fixed target marked by a black dot, a single moving anomaly is placed in a point of the domain and  $\Delta p$  is computed according to Eq.5. This process is then repeated for each point of the discretized domain to generate bi-dimensional maps illustrating the direction and magnitude of the movement of the moving anomaly computed by the proposed approach for the first step. In the left-hand column, the first guess conductivity variation of each voxel matches that of the target. A single voxel anomaly would be pushed toward the target, marked by a black dot. In the right-hand column, the first-guess conductivity variation of each voxel has the same amplitude as, but opposite sign to, the target. What was previously an attractor now becomes a repulsor. Two different locations of the target are considered in the first and second row. Arrows are normalized to the unit length for clarity of representation. The intensity of gray is proportional to the magnitude of the first step.

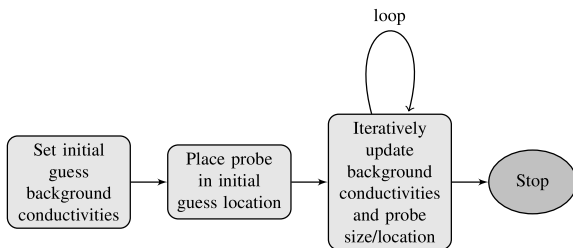


Fig. 3. Main steps of the parametric reconstruction algorithm

The electrical model is built and a user-defined number of electrodes is placed on the boundary of the region of interest. Since stroke is usually characterized by local anomalies in the brain region, we either employ a previous MRI scan of the subject (if available) or we register the subject's head to

a brain atlas in order to gather structural information on the location of the different tissues which are characterized by significantly different conductivities and exploit this information to enhance reconstruction. The surface potentials  $V_g$  are computed from an initial guess conductivity distribution and the measured surface potentials  $V_m$  are then used to calculate  $\Delta V = V_m - V_g$ . After Jacobian computation, inversion takes place and a variation of properties  $\Delta p$  is calculated. When TR is considered,  $\Delta p$  consists in a vector that specifies the conductivity variation of each voxel of the domain to be reconstructed; while in PAR  $\Delta p$  specifies the variation in conductivity of each background tissue as a whole and the variation in spatial coordinates and dimension of the moving anomaly. It is important to note that all the properties specified in the vector  $\Delta p$  are always simultaneously reconstructed at each step of the iterative inversion. If the stopping criterion is satisfied, the algorithm exits. Otherwise, new surface potentials

and Jacobian are calculated and the loop repeats itself.

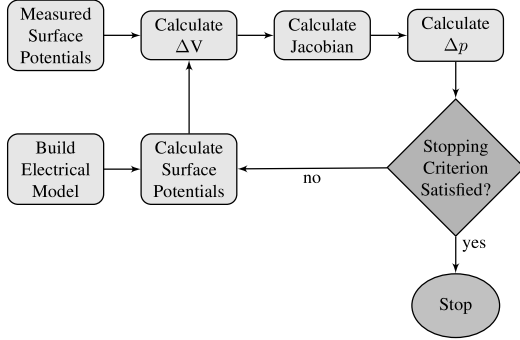


Fig. 4. General structure of an iterative EIT inversion algorithm.

#### A. Parametric Inversion

The position and dimension of the probe can vary inside definite boundaries set by the shape and dimension of the domain of interest.

In order to restrict the localization to the brain and CSF regions, in the example of stroke detection and discrimination considered, at each step the percentage of probe volume that overlaps brain tissue is computed and, if it is found to amount to less than 90%, the moving anomaly is moved towards the center of the head till it satisfies the requirement. Moreover, the radius of the probe has both upper and lower bounds. In particular, the radius of the guess anomaly reaching the lower limit is used as a stopping criterion identifying absence of the kind of stroke being examined.

Since the properties that can vary are simply the conductivities of the segmented tissues as a whole, the spatial coordinates of the center of the probe and its radius, in this case it pays to calculate the Jacobian with a finite-difference approach (Fig.5). The step for the spatial dimensions is 1 voxel and the one for tissue conductivity is set to 1% of the current conductivity value.

#### B. Tikhonov Based Inversion

The regularization parameter is selected by locating the point of maximum curvature on the L-curve generated by a one-step linear Gauss-Newton solver [50]. The iterative reconstruction stops when a local minimum of the error function is reached or the maximum number of iterations set by the user is met.

To detect and classify the conductivity anomaly, segmentation is performed by thresholding the reconstructed image with a threshold level computed as 75% of the maximum variation with respect to the initial guess condition. It is possible to correctly detect the absence of a target by considering only threshold levels above a minimum expected variation.

After labeling, any anomalies found are ranked according to their volume and those with a volume smaller than 20% of the largest detected anomaly are discarded to filter spurious lobes. If all the remaining anomalies differ from the background tissue in the same direction (increase or decrease

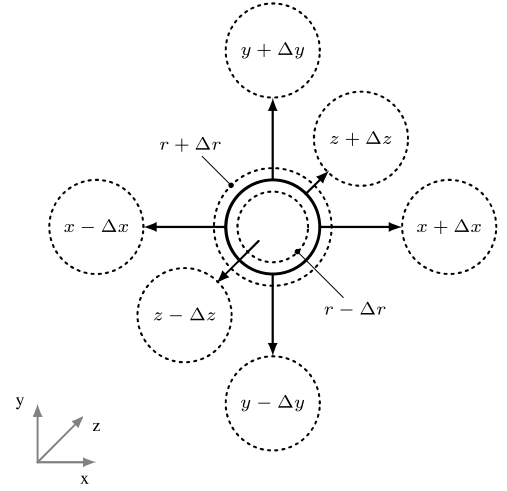


Fig. 5. Jacobian construction. The current position and size of the probe is depicted as a thick circle in the center of the image. The dotted lines represent the position and size of the anomaly used to calculate the Jacobian matrix.

in conductivity), then the stroke is classified as ischemic or hemorrhagic, depending on the conductivity of the detected region as compared to healthy tissue. Otherwise, no stroke is detected.

#### IV. EVALUATION OF PERFORMANCE

We now compare the detection and classification performances of the two algorithms, first in a cylindrical phantom, a commonly used benchmark for EIT reconstruction algorithms, and then on a simulated head volume to illustrate their behaviour in complex domains.

The computing system used in this work is specified in Table I, and was designed to provide high performance computing capabilities using low cost off-the-shelf components, leading to a system cost of less than 10K€ and relatively small size (4U rack mount).

CPU	2x Intel Xeon E5-2650 v2 @ 2.60GHz
GPU	4x Geforce GTX Titan Black
RAM	64 GB

TABLE I  
COMPUTING SYSTEM SPECIFICATIONS

##### A. Cylindrical Phantom Reconstructions

To test the newly developed algorithm and compare it to TR, we built a phantom consisting of a cylindrical polypropylene tank with radius  $r = 175$  mm containing 575 ml of saline solution. Sixteen equally spaced metal electrodes were placed on the boundary of the tank and four different opposite sinusoidal current injections at a frequency of 32 kHz were considered (see Fig. 6, first row). Each electrode consists of a 6 cm x 0.5 cm rectangular strip of aluminium tape (590 Series, 3M, U.S.A.) that spans from bottom to top of the vertical wall of the tank and is partially immersed in the saline solution. Four-terminal impedance measurements are performed with

the Agilent 4294A impedance analyzer (Agilent Technologies, U.S.A.) connected to a 16048H port extension cable [51]. In this case, only four opposite injections are considered in order to limit measurement drift due to the time required to manually acquire data with the impedance analyzer.

At the selected bandwidth level (4), frequency (32 kHz), oscillator level (500mV) and dc bias range (1mA), each data point is acquired in less than 100 ms and the SNR of the impedance measurement at the terminals of 16048H is approximately 54 dB [51], a value which is in the range of what is achievable with existing EIT systems [4], [52]. It has been verified that at the chosen frequency the noise at the electrode-solution interface is several orders of magnitude lower than the instrument noise, and is therefore neglected.

Four different conditions are considered: constant background conductivity ( $\sigma = 0.25$  [S/m]); two different locations of a single compact, uniform conductivity variation ( $\Delta\sigma = -0.25$  [S/m]) with radius  $r = 24$  mm; and the simultaneous presence of two compact, uniform conductivity variations ( $\Delta\sigma = -0.25$  [S/m] each) with radius  $r = 24$  mm (see Fig. 6, first row). In the following characterization, non-conductive cylindrical targets spanning the whole thickness of saline solution have been employed. Similar results have been experimentally obtained for background conductivities ranging from 0.15 to 0.35 [S/m] and non-conductive targets that do not span the whole thickness of saline solution and thus simulate only a localized partial reduction of conductivity.

The second row illustrates the reconstructions performed by PAR when the conductivity of the probe matches the actual target conductivity variation. If the conductivity of the probe is set to a value which is opposite in sign to the target conductivity variation, the reconstructions diverge, thus enabling correct classification. PAR can automatically detect more than one target without user input: after each convergent reconstruction the position and size of the reconstructed anomalies is fixed, an additional probe is placed inside the domain and a new inversion procedure is started. The process stops when the additional probe leads to a divergent reconstruction. As an example, in case of two different target contrasts simultaneously present in the domain, the first and second probes lead to convergent reconstructions in which the moving anomaly stops somewhere inside the domain with an above threshold radius. In contrast, the third probe has its radius reduced below threshold during the iterative inversion, thus leading to a divergent reconstruction.

The third row is relative to TR where the regularization parameter was optimized for each target position. In each column, the reconstructed conductivity variation is represented on the left-hand side, where dark shades of gray indicate a reduction in conductivity with respect to the background value and light shades the opposite. On the right-hand side, anomalies detected by the postprocessing procedure are highlighted in black or gray if the region is characterized by a significant reduction or increase of conductivity, respectively. Both algorithms perform equally well in the tested conditions.

To illustrate the importance of an appropriately adjusted regularization parameter  $\lambda$  for TR, in the fourth row it was reduced to 20% of the optimal value. While the L-curve op-

timization is straightforward for simple known setups such as the cylindrical phantom, in complex domains with significant geometrical uncertainties even larger discrepancies between the optimized and optimal values are to be expected [53]. It is apparent that both the raw reconstruction and the postprocessed data cannot be used to reliably detect and categorize a compact conductivity variation. If the regularization parameter is not properly tuned, the automated thresholding may misinterpret the image and classify the artifact as a real anomaly.

### B. Simulated Head Domain Reconstructions

The simulation setup, consisting in the electrical model and simulated measurements is initially described. The following subsections compare the performances of both algorithms in the presence of various sources of noise. Computational performances are then discussed.

1) *Electrical Model*: Segmentation and labeling of the MRI scan are performed by using BrainSuite, a collection of open source software tools that enable processing of magnetic resonance images (MRI) of the human brain [54].

The cubic mesh allows for a straightforward mapping between a 3 Tesla MRI scan and the electrical model, composed of cubic voxels, with sides 3 mm long. The scan is segmented in five layers: scalp, skull, connective tissue, CSF and brain. Table II presents the conductivities associated with each of the different tissues, the injection frequency being taken to be 8 KHz. Since at this frequency the complex conductivity has a real part that is from 20 (skin) to about 200 (blood) times larger than the imaginary part [45], the conductivity used in the electrical model is assumed for simplicity's sake to be real. The average conductivity of an ischemic stroke is set to 50% of the conductivity of the brain while a region associated with a hemorrhagic stroke is supposed to have a conductivity equal to that of the blood (Table II [45],[55][45]).

Tissue	Conductivity [S/m]
Scalp	0.2
Skull	0.02
Connective	0.385
CSF	2
Brain	0.13
Blood	0.7

TABLE II  
CONDUCTIVITIES OF THE DIFFERENT TISSUES

Electrodes are evenly distributed on the surface of the scalp. 128 measuring electrodes are considered and the injection pattern consists of 16 opposite injections [21]. Several techniques can be employed to quickly and accurately measure the positions of electrodes on the skin surface with an accuracy that is greater than the discretization considered in this work. Commonly applied methods include electromagnetic digitizers, ultrasound digitizers and geodesic photogrammetry systems [56] but new techniques can also take advantage of 3D laser scanners or computer vision [57].

2) *Simulated Measurements*: Three different situations are examined. The first one is a healthy condition where the

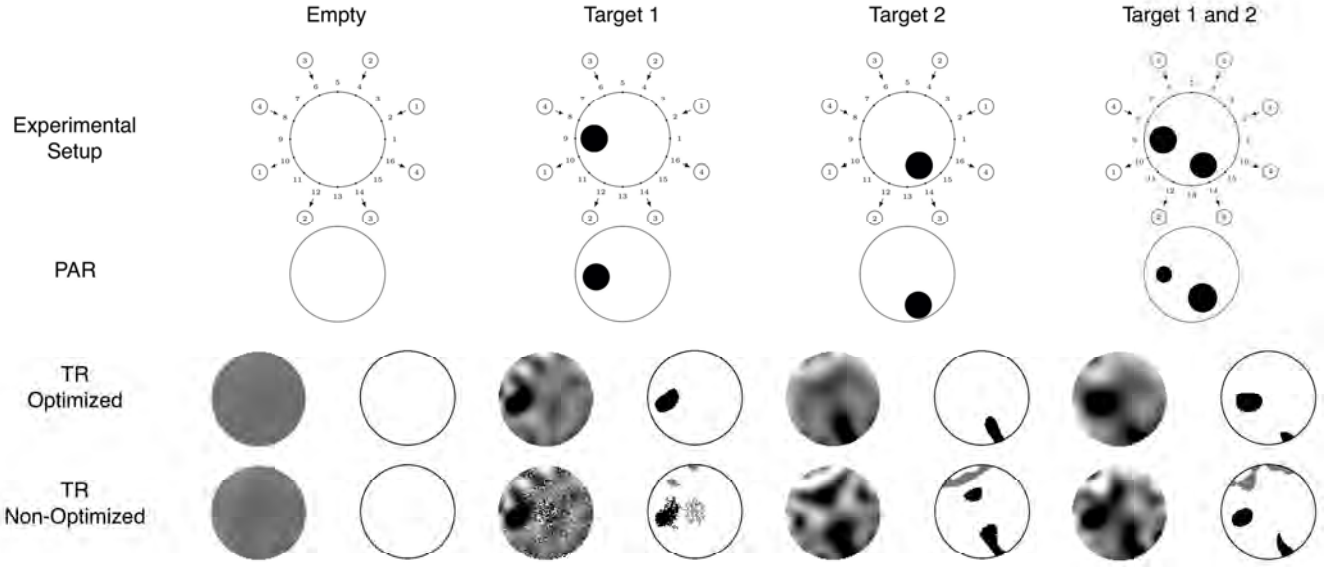


Fig. 6. Experimental results. The first row illustrates the experimental setup, composed of a cylindrical tank containing saline solution and cylindrical targets marked by black circles placed in various positions in the different columns. Sixteen electrodes are equally spaced on the border of the phantom and four different current injections, denoted by circled numbers, are sequentially applied. The second row shows the results of the reconstruction performed by the PAR algorithm, and the third one illustrates the conductivity variation reconstructed by TR and the anomalies recognized by means of the postprocessing procedure, where black and grey denote a significant reduction or increase in conductivity with respect to the background value, respectively. In the fourth row the reconstructions were performed with a regularization parameter that was approximately 20% of the optimized value.

conductivity is considered to be essentially uniform within each tissue. The other two possible conditions refer to the presence of a hemorrhagic or ischemic stroke, where a single target anomaly of ellipsoidal shape is placed at a specific location of the brain.

Four different sources of uncertainty are taken into consideration:

- 1) individual variations in tissue conductivity;
- 2) small scale conductivity inhomogeneities;
- 3) inaccurate segmentation;
- 4) electrical noise.

To model the individual variation in electrical properties, the conductivity of each segmented tissue  $t$  as a whole is considered to be affected by a random variation, modeled as:

$$\sigma_t = \sigma_t + \eta \cdot \sigma_t \quad (9)$$

where  $\sigma_t$  is the conductivity value of tissue  $t$  which is reported in the literature and  $\eta$  is a Gaussian distribution with average zero and standard deviation 0.1 [44].

Small-scale spatial fluctuations in the electrical properties of each segmented tissue and the stroke region are taken into account by considering the conductivity of each voxel to be affected by an additional random variation, modeled as:

$$\sigma_j = \sigma_j + \nu \cdot \sigma_j \quad (10)$$

where  $\sigma_j$  is the conductivity of voxel  $j$  and  $\nu$  is a Gaussian distribution with average value 0 and standard deviation 0.01.

The lack of exact knowledge as to head shape and tissue position is modeled by altering about 2.5% of each boundary between tissues, so that the electrical model considered in the

inversion step is structurally different from the one used to generate the simulated measurements. Focusing for example on the boundary between skin and air, the procedure consists in:

- 1) locating the skin voxels that border air voxels;
- 2) locating the air voxels that border skin voxels;
- 3) randomly turning 2.5% of each set of voxels to the neighboring tissue.

The robustness of EIT reconstruction algorithms to measurement noise is commonly tested with additive gaussian noise levels in the 0.1 to 10 percent range [20],[38],[58]. Thus, measurement noise modeled as a Gaussian random vector with mean 0 and standard deviation at two different levels, about 0.5% (low) and 5% (high) of the average amplitude of the simulated measurements, is finally added to the simulated measurements.

If we define our signal as the potentials at the electrodes when a stroke is present, the low and high noise levels correspond to SNRs (computed as the quadratic mean of the measurements referenced to the average) of about 48 and 28 dB, respectively. If, conversely, the signal is defined as the variation in electrode potentials in a stroke condition compared to a healthy one, the SNR depends on the position of the anomaly and its conductivity (see Table III, where P1, P2 and P3 represent three different locations).

Three different locations of a target anomaly of elliptical shape and both kinds of stroke are sequentially considered. The first target position (P1) is located between the parietal and occipital lobes of the left hemisphere, the second (P2) is placed in the frontal lobe slightly on the right side while

	Low Noise	High Noise
P1 Ischemic	17	-3
P1 Hemorrhagic	15	-5
P2 Ischemic	25	5
P2 Hemorrhagic	22	2
P3 Ischemic	14	-6
P3 Hemorrhagic	19	-2

TABLE III  
SNR STROKE - HEALTHY [DB]

the third one (P3) is placed in the temporal lobe of the left hemisphere (Fig. 7). The target anomaly is modeled as an

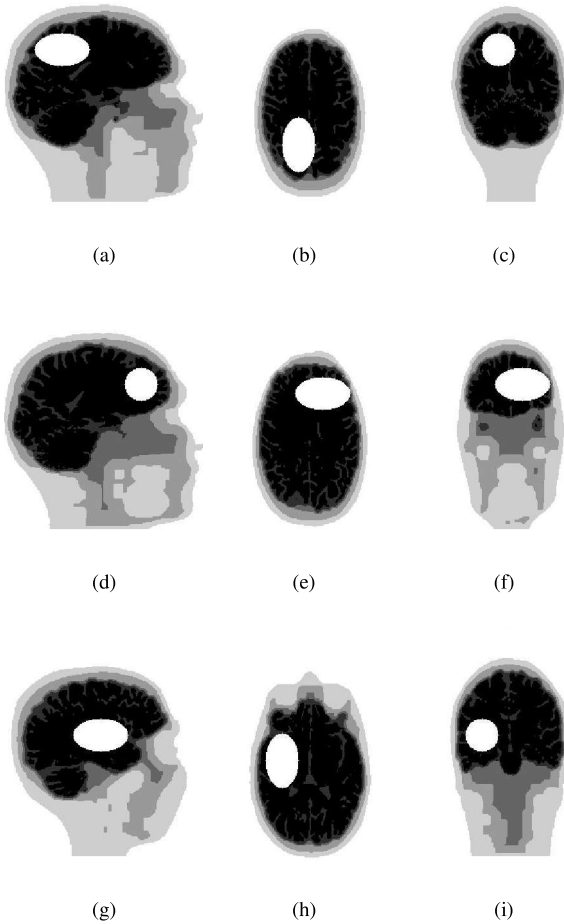


Fig. 7. Sagittal (a), (d) and (g); transverse (b), (e) and (h); and coronal (c), (f) and (i) sections passing through the center of the three target locations considered. Targets are illustrated as white ellipses and circles, which are sections of the 3D ellipsoid which simulates the generic structure of a compact stroke.

uniform elliptical contrast with volume  $V \approx 40 \text{ cm}^3$  [59] and conductivity variation that resembles either an ischemic or an hemorrhagic condition. Considering the fact that stroke severity is correlated with the volume of the affected brain tissue and that the intrinsic low resolution of impedance imaging makes it difficult to reliably detect small contrasts,

especially when significant uncertainty in the electrical model and measurement noise are present, we decided to focus on medium sized strokes which are more likely, if not promptly treated, to render the patient permanently dependent on other people to perform everyday activities [60].

To rank the performances of the algorithms, two different features are taken into account: the detection and the discrimination capabilities. Both are evaluated specifying, for each target considered as well as for the healthy condition, the percentage of strokes classified as ischemic, hemorrhagic or 'not detected'.

3) *PAR Reconstructions*: Ten different reconstructions, each with a different realization of electrical and tissue conductivity noise, are considered to produce the results illustrated in Fig. 8(a). In each reconstruction the lower radius bound for the moving probe is set to 5 voxels, corresponding to a volume of about  $14 \text{ cm}^3$  (about 33% of the actual target volume, which has an equivalent radius of 7 voxels), and both its shape (spherical) and initial volume ( $V \approx 57 \text{ cm}^3$ ) differ from the target anomaly. The higher radius bound, set to 15 voxels ( $V \approx 381 \text{ cm}^3$ ), was never reached during reconstructions thus it didn't affect the presented results.

Both kind of strokes are always correctly identified at all noise levels but some are not detected. At the lowest measurement noise level almost all the healthy conditions are correctly identified, however, a large amount of measurement noise makes the detection of healthy states unreliable. It is evident that increasing the electrical noise level leads to a degradation in detection performance for all the locations tested.

4) *TR Reconstructions*: In this case the reconstruction is limited to the brain and CSF regions and the conductivities of skin, skull and connective tissue are fixed at the correct values from literature data. Moreover, since the outermost tissues are not reconstructed by the TR algorithm, the noise due to possibly inaccurate segmentation is limited to the skin-air and CSF-brain boundaries. All the reconstructions are affected by the same noise realizations considered for PAR. The results are illustrated in Fig. 8(b).

In this case, even though the percentage of correct classifications is nearly always over 60% and as high as 100% in location P2, in all locations tested except P2 at least one realization leads to a wrong classification despite the significantly lower amount of uncertainty that affects the electrical model of the head in TR with respect to PAR.

Wrong classifications are present at both low and high electrical noise level, indicating that the main cause of misclassification is the noise affecting the electrical model of the head.

5) *PAR sensitivity to parameters*: During the reconstruction process the conductivity variation corresponding to the wandering probe is kept fixed at the values mentioned at the beginning of this section. If the conductivity variation due to the target differs from the fixed initial guess value of the wandering probe, then PAR compensates the discrepancy by varying the volume of the reconstructed region (see Fig. 9). Considering as an example position P3, if the target consists of an ischemic stroke with a conductivity difference that is 30%



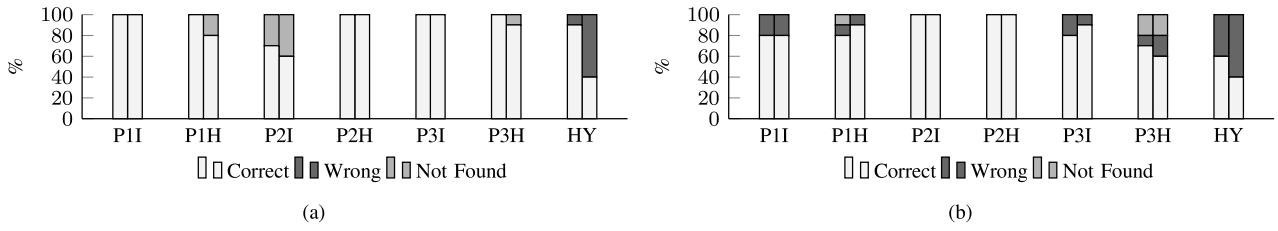


Fig. 8. Stroke detection and discrimination for each target location (P1, P2, P3) and kind (I: ischemic, H: hemorrhagic) and the healthy condition (HY) characterized by the absence of a target. For each group of two bars, the left one is relative to the low noise level (0.5%) while the right one depicts the results for the high noise level (5%). PAR inversion (a) and TR inversion (b).

smaller than the reference value, the algorithm converges upon a solution with a volume that is about 20% larger than would have been reconstructed for a target with nominal conductivity. The same happens when a hemorrhagic condition is present, though in this case the variation with respect to the background value is opposite in sign, so a decrease in target conductivity results in a decrease in the volume of the region reconstructed. Hence precise knowledge of the variation in conductivity due to a stroke condition is not a requirement for correct detection and classification. While generally not necessary for correct detection and classification, to obtain a unique solution and be able to distinguish the two extreme cases of very small inclusion with high conductivity variation and very large inclusion with small conductivity variation, a reasonable, but not accurate, guess about the electrical properties of the inclusion is needed.

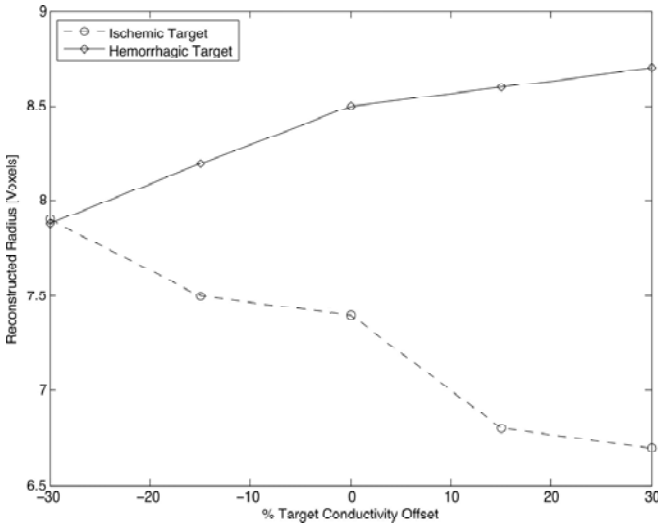


Fig. 9. A wrong assumption regarding the conductivity of the target region is compensated by the volume of the anomaly reconstructed. The points represent the average reconstructed radius of 10 noise realizations.

Fig. 10 illustrates how varying the minimum radius bound of the wandering probe affects the detection and discrimination performances of the PAR algorithm. In Fig. 10 (a) the parameter is lowered from 5 ( $V \approx 14 \text{ cm}^3$ ) to 4 voxels ( $V \approx 7 \text{ cm}^3$ ). As expected, the number of detections increases but the same happens to the number of incorrectly classified healthy conditions, due to the fact that a smaller reconstructed

inclusion is considered feasible. While at the lowest noise level tested each target is properly detected and classified, at the high noise level the algorithm misclassifies a hemorrhagic stroke in position P3. However, it is important to note that even the lowest noise level considered is easily achievable with existing EIT acquisition systems.

In contrast, in Fig. 10 (b), the minimum bound is increased from 5 ( $V \approx 14 \text{ cm}^3$ ) to 6 voxels ( $V \approx 24 \text{ cm}^3$ ). In this case, as the size of the minimum feasible detection is increased, the number of detected targets is lower when compared to the results obtained with the nominal parameter in Fig. 8 (a). The upside is a better classification performance for healthy conditions.

As illustrated, the detection and classification performances of the PAR algorithm vary according to the selected minimum bound of the wandering probe, however, for a realistic amount of measurement noise, PAR still manages to avoid the misclassification of the detected targets. This is very significant for the presented case study of stroke detection and classification because tPA administration to a hemorrhagic patient may well aggravate his condition.

### C. Computational Performances

In the general case, each iteration of TR requires computation of  $N_e \cdot N_i$  forward problems and solution of (8), where  $J^T \cdot J + \Gamma^T \cdot \Gamma$  is a matrix whose number of elements in the head domain is in the order of  $10^9$ . In PAR,  $N_i \cdot (2 \cdot N_k + 1) \cdot N_g$  forward problem solutions are computed for each iteration and the small matrix  $J_p^T \cdot J_p$ , with a number of elements in the order of 10, is inverted at each step as in (5). It is worth noting that in this case the number of forward problems does not depend on the number of measuring electrodes  $N_e$  but is related only to the number of different injections  $N_i$ , different properties  $N_k$  that are varied in the reconstruction process (5 tissues and 4 spatial parameters that define the position and dimension of the moving anomaly, in the example considered) and the number of initial guess locations of the moving anomaly  $N_g$ .

A typical 3D setting for the application of stroke detection considered consists of an acquisition system supporting 128 electrodes and an injection pattern composed of 16 different injections. In this case the number of forward problems solved for each iteration is 2048 for TR while for PAR it is 2432.

In the configurations tested, the number of forward problem solutions needed for each iteration is similar for both methods



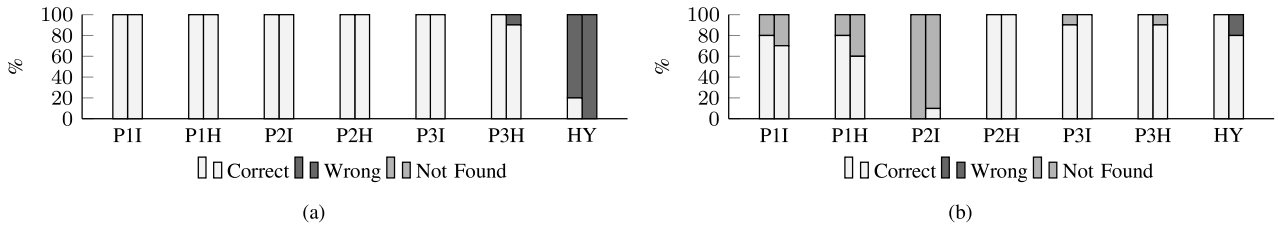


Fig. 10. Detection and classification performances of the PAR algorithm when the minimum radius of the wandering probe is set to 4 voxels (a) and 6 voxels (b). The results are relative to each target location (P1, P2, P3) and kind (I: ischemic, H: hemorrhagic) and the healthy condition (HY) which is characterized by the absence of a target. For each group of two bars, the left one is relative to the low noise level (0.5%) while the right one depicts the results for the high noise level (5%).

and PAR has a speed advantage over TR due to the much smaller Jacobian matrix  $J_p$  and the absence of a critical regularization parameter that needs to be tuned for the specific domain and noise realization. The small  $J_p$  of PAR is also quick to construct, with the time required basically consisting of the necessary forward problem solutions, whereas the implementation of the reciprocity principle for the construction of  $J$  in TR is computationally expensive.

In large scale problems such as the present case study of stroke detection, a generalized SVD analysis of the reconstruction as a function of the regularization parameter or methods based on the computation of the condition number [61] are prohibitive, and thus the L-curve is generally computed only at a few points corresponding to discrete values of the regularization parameter and the value that leads to the point of maximum curvature is selected [50]. In our experience, at least 10 different points are needed to obtain a good approximation of the L-curve in the application considered. This is a significant drawback of regularized methods because in real-life measurements the sources of noise are multiple and generally not precisely characterized, so in large-scale problems it is difficult to quickly determine a good value for  $\lambda$ .

In our system (see Table I), with the previously considered 3D volume consisting of a segmented head discretized with 125850 voxels, each with a volume of  $27 \text{ mm}^3$ , the average time required for stroke detection and discrimination is 24 minutes for PAR and 105 minutes for TR (Fig. 11), thus PAR provides a speedup greater than 4X over TR. Each forward problem computation requires about 0.2 seconds; the time needed for the implementation of the reciprocity principle in TR is about 15 minutes; the inversion step in TR (8) takes about three minutes for each iteration, while in PAR (5) it is nearly instantaneous, and the postprocessing procedure enabling automatic detection and classification of conductivity contrasts for TR requires about 15 seconds for each inversion process. The average number of inversion steps is 3 for both methods and, for TR, the overhead due to optimization of the regularization parameter amounts to an additional 30 minutes.

It is important to note that, in applications in which the direction of the conductivity variation due to target with respect to background is known a priori, the number of forward problem solutions and inversion steps for PAR is roughly halved. Another important advantage of the proposed

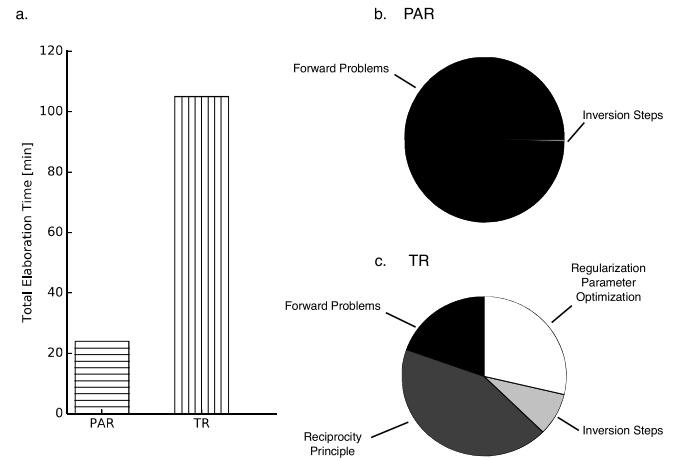


Fig. 11. a) average time for stroke detection and discrimination. For the considered task PAR is more than 4X quicker than TR. b), d) pie charts detailing how the total reconstruction time is split among the main inversion modules for PAR and TR, respectively. The absence of a regularization parameter which needs to be optimized, a simple Jacobian construction and a light inversion step give PAR a significant speed advantage over TR.

algorithm concerns the scalability of the inversion to meshes with a large number of elements. Since the reconstruction is parametric and not voxel by voxel, the computational cost of the inversion step is independent of the number of discretizing elements.

#### D. Limitations

The aim of the proposed approach, PAR, is not precise estimation of position and size of the target conductivity contrasts but only their quick detection and classification as increase or decrease of conductivity with respect to the background. PAR is compared with an implementation of TR which is combined with a postprocessing procedure that allows automatic detection and classification of conductivity contrasts. In applications where accurate localization and amplitude estimation are of main importance, while computational cost and time to reconstruction are not a concern, sparsity regularization techniques may provide finer spatial resolution.

The results presented in Fig. 8 demonstrate that PAR is able to tolerate a level of background inhomogeneity which

is consistent with the one present in the considered case study. Nonetheless, in other potential applications a high-contrast distributed inhomogeneous background (e.g. stripy or grid like) may generate additional local minima and increase the number of not found and wrong classifications for both presented algorithms. In those cases, subdomain techniques may be more appropriate.

While PAR has been tested extensively in several conditions, both experimentally using phantoms and in simulated complex 3D domains affected by both significant uncertainty in the electrical model and considerable measurement noise, theoretical proof of convergence in all cases is still not available. Given the various sources of noise that affect EIT measurements in practical applications, the analysis is focused on an empirical evaluation of robustness with respect to several sources of uncertainty.

PAR can automatically detect multiple targets by embedding the probe in the electrical model after each convergent reconstruction and by running additional reconstructions until the radius of the last probe is smaller than threshold. As the first detection tends to partly compensate for the presence of other targets, it tends to be larger than the actual object. This process might lead to the misdetection of a few very small targets, especially if significant noise is present. For the considered application of stroke detection and discrimination, simultaneous presence of ischemic and hemorrhagic conditions is very rare [62] and reconstructions are in principle not affected by the previously described potential misdetection mechanism due to the opposite variations with respect to the background. Moreover, acute pharmacological treatment is not dependent on the precise number of strokes of the same kind [63], so in this case the misdetection of a few very small contrasts is not critical. Nonetheless, the detection of a mixture of small and large targets may be of interest in other applications, and the authors consider a thorough characterization of detection performance in presence of several small target contrasts, for both presented algorithms, an interesting development to be included in a future work.

While both algorithms were tested with the same electrical model discretization, to allow for an unbiased comparison, further work is needed to assess the minimum number of mesh elements required for good detection and discrimination performance in the considered case study.

In the previous analysis it is assumed that the conductivity contrast to be detected and classified can be appropriately approximated by a spherical probe. While the probe is spherical, non spherical target contrasts have been tested. As demonstrated by the results obtained with the simulated 3D head domain, where the target is an ellipsoid while the wandering probe is spherical, PAR is able to correctly detect and classify compact conductivity contrasts of unknown shape. As a first paper on the topic, the analysis is limited to ellipsoidal targets. As a future development, the authors plan to test the reconstruction performance in presence of markedly irregular target contrasts.

## V. CONCLUSIONS

In this work, a special purpose imaging technique for EIT, targeting the automatic recognition and classification of compact conductivity anomalies, has been presented. PAR does not follow the usual approach of reconstructing a complete conductivity map of the region of interest on a voxel by voxel basis, but instead resorts to a new strategy: it exploits additional information given by the specific constraints of the application to reduce the number of unknowns and efficiently detect and classify a target without focusing on its shape.

Very often in practical applications, and in the case study considered, the actual conductivity of the various volumes that compose the domain and their boundaries are not precisely known; thus separating reconstruction of the background regions from detection of a compact conductivity contrast (identified by its size and location) is advantageous and leads to reliable recognition of the target over a wider range of conditions.

For the considered application, PAR proves to be quicker and more robust than widely employed voxel by voxel regularized inversion methods, in particular when complex 3D electrical models are required and significant discretization and measurement noises are present, such as in stroke detection and discrimination. While the gold standard for early stroke detection remains MRI, EIT may be quickly employed in the field well before an MRI scanner is available for definitive diagnosis. The proposed approach may reduce the time to detection, at least for a subset of cases, thus leading to an increase in the number of patients able to receive treatment in the narrow timeframe available for tPA.

Additionally, it has been shown how the algorithm proposed is capable of compensating for erroneous assumptions as to the conductivity and target shape, making the algorithm robust in the presence of anomalies with unknown (compact) shapes and electrical properties.

The reduced computational burden and the absence of a critical regularization parameter make application of the parametric reconstruction method a promising alternative for quick detection and characterization of compact conductivity variations.

## REFERENCES

- [1] M. Lukashewitsch, P. Maass, and M. Pidgeon, "Tikhonov regularization for electrical impedance tomography on unbounded domains," *Inverse problems*, vol. 19, p. 585, 2003.
- [2] T. York, "Status of electrical tomography in industrial applications," *Journal of Electronic Imaging*, vol. 10, p. 608, Jul. 2001.
- [3] D. Silvera-Tawil *et al.*, "Electrical impedance tomography for artificial sensitive robotic skin: A review," 2014.
- [4] R. Bayford, "Bioimpedance tomography (electrical impedance tomography)," *Annu. Rev. Biomed. Eng.*, vol. 8, pp. 63–91, Aug 2006.
- [5] J. Mueller, D. Isaacson, and J. Newell, "Reconstruction of conductivity changes due to ventilation and perfusion from eit data collected on a rectangular electrode array," *Physiological Measurement*, vol. 22, p. 97, 2001.
- [6] N. Vaisman, N. Weintrob, and A. Blumental, "Gastric emptying in patients with type i diabetes mellitus," *Annals of the New York Acad. Sci.*, 1999.
- [7] R. Halter, A. Hartov, and K. Paulsen, "A broadband high-frequency electrical impedance tomography system for breast imaging," *Biomedical Engineering, IEEE Transactions on*, vol. 55, pp. 650–659, 2008.
- [8] H. Syed *et al.*, "Anatomically accurate hard priors for transrectal electrical impedance tomography (treit) of the prostate," *Physiological Measurement*, vol. 33, p. 719, 2012.

- [9] T. Tidswell *et al.*, "Three-dimensional electrical impedance tomography of human brain activity," *NeuroImage*, vol. 13, pp. 283–294, Feb. 2001.
- [10] M. Guermandi *et al.*, "Active electrode ic combining eeg, electrical impedance tomography, continuous contact impedance measurement and power supply on a single wire," *IEEE Trans. Biomed. Circuits Sys.*, pp. 335–338, 2011.
- [11] B. Packham, H. Koo, and A. Romsauerova, "Comparison of frequency difference reconstruction algorithms for the detection of acute stroke using EIT in a realistic head-shaped tank," *Physiological Measurement*, 2012.
- [12] D. Holder, *Electrical impedance tomography: methods, history and applications*. Institute of Physics Publishing, 2004.
- [13] M. T. Clay and T. C. Ferree, "Weighted regularization in electrical impedance tomography with applications to acute cerebral stroke," *IEEE Trans. Med. Imag.*, vol. 21, pp. 629–637, Jan 2002.
- [14] S. M. Davis and G. A. Donnan, "4.5 hours: The new time window for tissue plasminogen activator in stroke," *Stroke*, vol. 40, pp. 2266–2267, Jun 2009.
- [15] I. Marinkovic *et al.*, "Evolution of intracerebral hemorrhage after intravenous tpa: reversal of harmful effects with mast cell stabilization," *Journal of Cerebral Blood Flow & Metabolism*, vol. 34, pp. 176–181, 2014.
- [16] E. Malone *et al.*, "Stroke type differentiation using spectrally constrained multifrequency eit: evaluation of feasibility in a realistic head model," *Physiological Measurement*, vol. 35, pp. 1051–1066, May 2014.
- [17] A. Romsauerova *et al.*, "Multi-frequency electrical impedance tomography (eit) of the adult human head: initial findings in brain tumours, arteriovenous malformations and chronic stroke, development of an analysis method and calibration," *Physiological Measurement*, vol. 27, pp. S147–S161, Apr. 2006.
- [18] A. Nissinen, L. M. Heikkinen, and J. P. Kaipio, "The Bayesian approximation error approach for electrical impedance tomography—experimental results," *Measurement Science and Technology*, vol. 19, p. 015501, Nov. 2007.
- [19] A. Nissinen, V. P. Kolehmainen, and J. P. Kaipio, "Compensation of Modelling Errors Due to Unknown Domain Boundary in Electrical Impedance Tomography," *IEEE transactions on medical imaging*, vol. 30, pp. 231–242.
- [20] A. Nissinen *et al.*, "Contrast enhancement in EIT imaging of the brain," *Physiological Measurement*, pp. 1–24, Dec. 2015.
- [21] A. McEwan *et al.*, "Design and calibration of a compact multi-frequency eit system for acute stroke imaging," *Physiological Measurement*, vol. 27, p. S199, 2006.
- [22] D. Freimark *et al.*, "Monitoring lung fluid content in CHF patients under intravenous diuretics treatment using bio-impedance measurements," *Physiological Measurement*, vol. 28, pp. S269–S277, Jun. 2007.
- [23] A. Tamburrino and G. Rubinacci, "A new non-iterative inversion method for electrical resistance tomography," *Inverse problems*, 2002.
- [24] F. Ries, T. D. Marco, and R. Guerrieri, "Tuning solution of large non-hermitian linear systems on multiple graphics processing unit accelerated workstations," *International Journal of High Performance Computing Applications*, vol. 26, pp. 296–309, 2012.
- [25] M. Chiesi *et al.*, "Power-aware job scheduling on heterogeneous multicore architectures," *IEEE Trans. Parallel Distrib. Syst.*, vol. 26, pp. 868–877, Mar 2015.
- [26] X. Zhang *et al.*, "An image reconstruction algorithm for 3d electrical impedance mammography," *IEEE Trans. Med. Imag.*, vol. 33, pp. 2223–2241, 2014.
- [27] M. Cheney, D. Isaacson, and J. Newell, "Electrical impedance tomography," *SIAM review*, vol. 41, pp. 85–101, 1999.
- [28] F. Santosa and M. Vogelius, "A backprojection algorithm for electrical impedance imaging," *SIAM Journal on Applied Mathematics*, 1990.
- [29] H. Wang, C. Wang, and W. Yin, "A Pre-Iteration Method for the Inverse Problem in Electrical Impedance Tomography," *IEEE Transactions on Instrumentation and Measurement*, vol. 53, pp. 1093–1096, Aug. 2004.
- [30] T. J. YORKEY, J. G. WEBSTER, and W. J. TOMPKINS, "Comparing Reconstruction Algorithms for Electrical-Impedance Tomography," *IEEE Transactions on Biomedical Engineering*, vol. 34, pp. 843–852, Nov. 1987.
- [31] W. R. B. Lionheart, "Eit reconstruction algorithms: pitfalls, challenges and recent developments," *Physiological Measurement*, vol. 25, pp. 125–42, Feb 2004.
- [32] M. Vauhkonen *et al.*, "Tikhonov regularization and prior information in electrical impedance tomography," *IEEE Trans. Med. Imag.*, vol. 17, pp. 285–293, 1998.
- [33] A. Borsic *et al.*, "Total variation regularization in electrical impedance tomography," 2007.
- [34] M. Gehre *et al.*, "Journal of Computational and Applied Mathematics," *Journal of Computational and Applied Mathematics*, vol. 236, pp. 2126–2136, Feb. 2012.
- [35] J. Zhao *et al.*, "A fast sparse reconstruction algorithm for electrical tomography," *Measurement Science and Technology*, 2014.
- [36] S. I. Kang *et al.*, "A sub-domain based regularization method with prior information for human thorax imaging using electrical impedance tomography," *Measurement Science and Technology*, pp. 1–9, Nov. 2016.
- [37] L. Miao, Y. Ma, and J. Wang, "ROI-Based Image Reconstruction of Electrical Impedance Tomography Used to Detect Regional Conductivity Variation," *IEEE Transactions on Instrumentation and Measurement*, vol. 63, pp. 2903–2910, 2014.
- [38] S. I. Kang *et al.*, "EIT image reconstruction for two-phase flow monitoring using a sub-domain based regularization method," *Flow Measurement and Instrumentation*, 2016.
- [39] B. Gong *et al.*, "Sparse regularization for EIT reconstruction incorporating structural information derived from medical imaging," *Physiological Measurement*, pp. 843–862, Nov. 2016.
- [40] M. Glidewell and K. Ng, "Anatomically constrained electrical impedance tomography for three-dimensional anisotropic bodies," *Medical Imaging, IEEE Transactions on*, vol. 16, pp. 572–580, 1997.
- [41] M. Clay and T. Ferree, "Weighted regularization in electrical impedance tomography with applications to acute cerebral stroke," *Medical Imaging*, 2002.
- [42] B. Brandstatter, "Jacobian calculation for electrical impedance tomography based on the reciprocity principle," *Magnetics, IEEE Transactions on*, vol. 39, pp. 1309–1312, 2003.
- [43] C. Gabriel, S. Gabriel, and E. Corthout, "The dielectric properties of biological tissues: I. Literature survey," *Physics in Medicine and Biology*, vol. 41, p. 2231, 1996.
- [44] S. Gabriel, R. Lau, and C. Gabriel, "The dielectric properties of biological tissues: II. measurements in the frequency range 10 hz to 20 ghz," *Physics in Medicine and Biology*, vol. 41, p. 2251, 1996.
- [45] —, "The dielectric properties of biological tissues: III. parametric models for the dielectric spectrum of tissues," *Physics in medicine and biology*, vol. 41, p. 2271, 1996.
- [46] P. Hasgall *et al.*, "It's database for thermal and electromagnetic parameters of biological tissues," [www.itis.ethz.ch/database](http://www.itis.ethz.ch/database), September 2015, version 3.0 DOI: 10.13099/VIP21000-03-0.
- [47] R. D. Zimmerman and J. A. Maldjian, "Radiologic estimation of hematoma volume in intracerebral hemorrhage trial by CT scan," *American journal ...*, 2006.
- [48] G. Golub, P. Hansen, and D. O'Leary, "Tikhonov regularization and total least squares," *SIAM Journal on Matrix Analysis and Applications*, vol. 21, pp. 185–194, 1999.
- [49] T. D. Marco *et al.*, "Eit forward problem parallel simulation environment with anisotropic tissue and realistic electrode models," *IEEE Trans. Med. Imag.*, vol. 59, pp. 1229–1239, 2012.
- [50] P. C. Hansen and D. P. OLEARY, "The use of the l-curve in the regularization of discrete ill-posed problems," *SIAM Journal on Scientific Computing*, vol. 14, pp. 1487–1503, Nov. 1993.
- [51] Agilent 4294A Precision Impedance Analyzer Data Sheet, Jan 2003.
- [52] L. Fabrizi *et al.*, "Analysis of resting noise characteristics of three eit systems in order to compare suitability for time difference imaging with scalp electrodes during epileptic seizures," *Physiological Measurement*, vol. 28, pp. S217–S236, Jun 2007.
- [53] P. R. Johnston and R. M. Gulrajani, "Selecting the corner in the l-curve approach to tikhonov regularization," *IEEE Transactions on Biomedical Engineering*, vol. 47, pp. 1293–1296, 2000.
- [54] D. Shattuck and R. Leahy, "Brainsuite: an automated cortical surface identification tool," *Medical image analysis*, vol. 6, pp. 129–142, 2002.
- [55] H. PA *et al.*, *IT'IS Database for thermal and electromagnetic parameters of biological tissues. Version 3.0*, Sep 2015.
- [56] L. Koessler *et al.*, "Spatial localization of eeg electrodes," *Neurophysiologie Clinique/Clinical Neurophysiology*, vol. 37, pp. 97–102, Apr. 2007.
- [57] M. Pechaud *et al.*, "Automatic labeling of eeg electrodes using combinatorial optimization," in *29th Annual International Conference EMBC 2007*, 2007, pp. 4398–4401.
- [58] E. Lee *et al.*, "Breast EIT using a new projected image reconstruction method with multi-frequency measurements," *Physiological Measurement*, vol. 33, pp. 751–765, Apr. 2012.
- [59] P. Pantano *et al.*, "Delayed increase in infarct volume after cerebral ischemia correlations with thrombolytic treatment and clinical outcome," *Stroke*, 1999.

- [60] D. Saunders, A. Clifton, and M. Brown, "Measurement of infarct size using MRI predicts prognosis in middle cerebral artery infarction," *Stroke*, vol. 26, pp. 2272–2276, 1995.
- [61] D. Watzenig, B. Brandstatter, and G. Holler, "Adaptive Regularization Parameter Adjustment for Reconstruction Problems," *IEEE Transactions on Magnetics*, vol. 40, pp. 1116–1119, Mar. 2004.
- [62] K. Balci *et al.*, "Simultaneous Onset of Hemorrhagic and Ischemic Strokes," *The Neurologist*, vol. 13, pp. 148–149, May 2007.
- [63] Y. Ueno *et al.*, "Mobile Aortic Plaques Are a Cause of Multiple Brain Infarcts Seen on Diffusion-Weighted Imaging," *Stroke*, vol. 38, pp. 2470–2476, Aug. 2007.